A fast bar in the post-interaction galaxy NGC 1023

Victor P. Debattista,[1]★ Enrico Maria Corsini[2] and J. A. L. Aguerri[1]

[1]*Astronomisches Institut, Universität Basel, Venusstrasse 7, CH-4102 Binningen, Switzerland*
[2]*Osservatorio Astrofisico di Asiago, Dipartimento di Astronomia, Università di Padova, via dell'Osservatorio 8, I-36012 Asiago, Italy*

ABSTRACT

We measured the bar pattern speed, Ω_p, of the SB0 galaxy NGC 1023 using the Tremaine–Weinberg method with stellar-absorption slit spectroscopy. The morphology and kinematics of the H I gas outside NGC 1023 suggest it suffered a tidal interaction, sometime in the past, with one of its dwarf companions. At present, however, the optical disc is relaxed. If the disc had been stabilized by a massive dark matter halo and formed its bar in the interaction, then the bar would have to be slow. We found $\Omega_p = 5.0 \pm 1.8 \, \text{km s}^{-1} \, \text{arcsec}^{-1}$, so that the bar ends near its corotation radius. It is therefore rotating rapidly and must have a maximum disc.

Key words: galaxies: elliptical and lenticular, cD – galaxies: haloes – galaxies: individual: NGC 1023 – galaxies: interactions – galaxies: kinematics and dynamics – galaxies: photometry.

1 INTRODUCTION

Strong bars are seen in optical images of roughly 30 per cent of all high surface brightness (HSB) disc galaxies (Sellwood & Wilkinson 1993) and this fraction rises to 50–75 per cent in the near IR (Knapen 1999; Knapen, Shlosman & Peletier 2000; Eskridge et al. 2000). Understanding the structure and dynamics of barred (SB) galaxies is, therefore, an issue of some importance. The principal dynamical quantity for SB galaxies is the rotation frequency/pattern speed of the bar, Ω_p. This is usually parametrized by the distance-independent ratio $\mathcal{R} \equiv D_L/a_B$, where a_B is the semi-major axis of the bar and D_L is the radius to the Lagrangian point, where the gravitational and centrifugal forces cancel out in the bar's rest frame. (The Lagrangian radius is therefore the generalization to strong bars of the corotation radius.) Contopoulos (1980) argued that a self-consistent bar is possible only if $\mathcal{R} \geqslant 1$. A bar is termed fast when $1.0 \leqslant \mathcal{R} \leqslant 1.4$, while, for a larger value of $\mathcal{R}$, a bar is said to be slow.

A variety of methods have been used to attempt measurement of bar pattern speeds (see, for example, the review of Elmegreen 1996). Most measurements of $\mathcal{R}$ rely on hydrodynamical simulations. These usually try to match the gas flow in the region of the bar, particularly at the shocks, which works because the location of the shocks depends on $\mathcal{R}$, moving further ahead of the bar as $\mathcal{R}$ increases. A bar needs to be fast for the shocks to remain curved with their concave sides towards the bar major axis, as is usually observed (van Albada & Sanders 1982; Athanassoula 1992). Detailed simulations of gas flows in individual galaxies also result in fast bars; examples include: NGC 1365 ($\mathcal{R} = 1.3$, Lindblad, Lindblad & Athanassoula 1996), NGC 1300 ($\mathcal{R} = 1.3$,

Lindblad & Kristen 1996), and NGC 4123 ($\mathcal{R} = 1.2$, Weiner, Sellwood & Williams 2001). Hydrodynamical simulations can also recover $\mathcal{R}$ by matching morphological features in H I; some examples are NGC 7479 ($\mathcal{R} = 1.22$, Laine 1996), NGC 1073 ($\mathcal{R} = 1$–1.2, England, Gottesman & Hunter 1990), NGC 3992 ($\mathcal{R} = 1$, Hunter et al. 1989), and NGC 5850 ($\mathcal{R} = 1.35$, Aguerri et al. 2001).

A direct method for measuring Ω_p, using a tracer population which satisfies continuity, was developed by Tremaine & Weinberg (1984). Since gas is subject to phase changes, it is not well suited for this application. Old stellar populations in the absence of significant obscuration, on the other hand, are ideal for the Tremaine–Weinberg (TW) method. This has permitted application of the method to a small number of early type SB galaxies: NGC 936 ($\mathcal{R} = 1.4 \pm 0.3$, Kent 1987 and Merrifield & Kuijken 1995), NGC 4596 ($\mathcal{R} = 1.15^{+0.38}_{-0.23}$, Gerssen et al. 1999) and NGC 7079 ($\mathcal{R} = 0.9 \pm 0.15$, Debattista & Williams 2001).

The observational evidence, therefore, favours fast bars. The perturbation theory calculations of Weinberg (1985) predicted that a fast bar would be slowed down rapidly in the presence of a massive dark matter (DM) halo. Such slow-down has been seen in various simulations (Sellwood 1980; Little & Carlberg 1991; Hernquist & Weinberg 1992; Athanassoula 1996). The fully self-consistent, high resolution N-body simulations of Debattista & Sellwood (1998) also confirmed this prediction; however they showed that, for a maximum disc (here taken to mean a disc which dominates the rotation curve throughout the inner few disc scalelengths, cf. van Albada & Sancisi 1986), a fast bar can survive for a large fraction of a Hubble time. Subsequently, Tremaine & Ostriker (1999) suggested that bars manage to remain fast not because discs are maximal but rather because the inner parts of DM haloes are flattened and rapidly rotating. However, Debattista &

Table 1. Log of the surface photometry observations.

Filter	Date	t_{exp} (s)
B	27 Dec 2000	3×900
	28 Dec 2000	900
V	28 Dec 2000	4×480
I	27 Dec 2000	20×180
	28 Dec 2000	10×180

Sellwood (2000) showed that rapid slow-down persists even then unless the halo angular momentum is very large relative to that of the disc. Thus they concluded that SB galaxies must be maximal, and argued that the same must be true for all high surface brightness disc galaxies.

This conclusion rests on a small number of pattern speed measurements; in view of the fact that maximum discs are in conflict with the predictions of cold dark matter (CDM) cosmologies (e.g. Navarro, Frenk & White 1997), enlarging the sample of measured pattern speeds is desirable. In this paper, we report observations of NGC 1023, for which we applied the TW method.

The rest of this paper is organized as follows. The TW method is described briefly in Section 2. Then, in Section 3 we give an overview of the previously known properties of NGC 1023. The photometric observations, reduction and results, including a_B, are presented in Section 4, while Section 5 presents the spectroscopic observations and results. We derive the rotation curve, corrected for the asymmetric drift, from which we obtain D_L. With these results at hand, we then apply the TW method in Section 6. We present our conclusions in Section 7.

2   THE TREMAINE–WEINBERG METHOD

The TW method is contained in the following simple equation:

$$\Omega_p \sin i = \frac{\int_{-\infty}^{\infty} h(Y) \int_{-\infty}^{\infty} \Sigma(X, Y) V_{los}(X, Y) \, dX \, dY}{\int_{-\infty}^{\infty} h(Y) \int_{-\infty}^{\infty} \Sigma(X, Y) X \, dX \, dY}, \qquad (1)$$

where i is the inclination of the galaxy, V_{los} is the line-of-sight (minus systemic) velocity, Σ is the surface brightness, h is an arbitrary weighting function and (X, Y) are coordinates on the sky, centred on the galaxy, along the apparent major and minor axes of the disc, respectively. Slit observations are equivalent to $h(Y) \propto \delta(Y - Y_{slit})$. Application of equation 1 presents three main difficulties.

(i) *Centring errors.* As was already recognized by Tremaine & Weinberg (1984), small errors in identifying either the centre or the systemic velocity of the galaxy can significantly affect the value of Ω_p obtained. Noting that most SB galaxies are nearly point-symmetric about their centres, Tremaine & Weinberg (1984) suggested using a weighting function which is odd in Y to counter this problem. Merrifield & Kuijken (1995) used a different, and somewhat better, strategy. Noting that the integrals in equation 1 represent luminosity-weighted averages, they rewrote equation 1 as

$$\Omega_p \sin i (\mathcal{X} - X_c) = \mathcal{V} - V_{sys}, \qquad (2)$$

where $\mathcal{V}$ and $\mathcal{X}$ are the luminosity-weighted averages relative to an arbitrary frame, in which the galaxy centre is (X_c, Y_c) and the
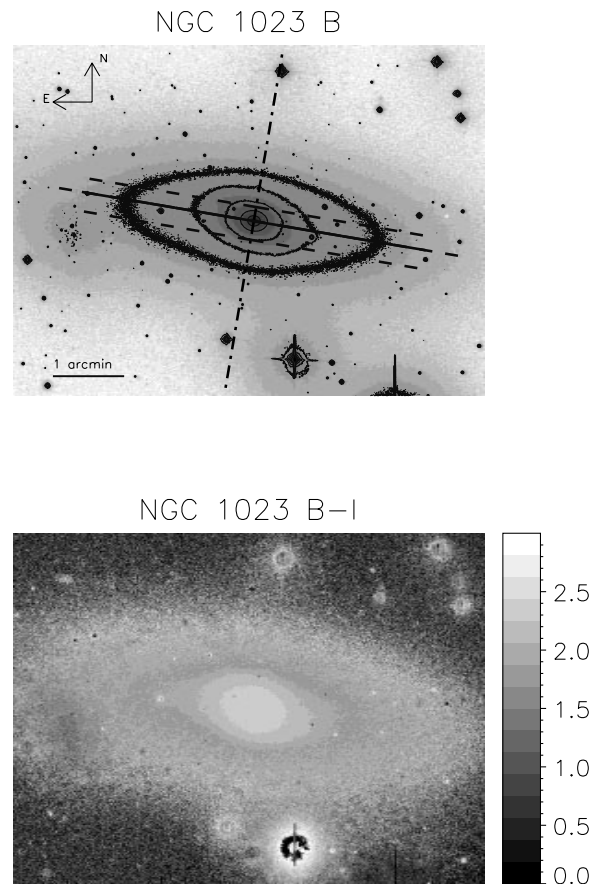

NGC 1023 B

NGC 1023 B−I

Figure 1. The *B*-band image (top) and $B - I$ colour map (bottom) of NGC 1023. In the *B*-band image, the overplotted full line is the major axis (PA = 80°.2), while the minor axis is indicated by the dot-dashed line. The offset slits, parallel to the major axis and shifted by 12 arcsec to the north and 16 arcsec to the south, are shown by dashed lines. The companion galaxy NGC 1023A can be seen to the east, just south of the major axis. The contour levels shows are $\mu_B = 18$ to 22 mag arcsec^{-2}, at unit intervals, with the outermost contour being $\mu_B = 22$ mag arcsec^{-2}. The $B - I$ map shows that the strongest colour variations are associated with the bulge (which is red) and NGC 1023A (which is blue).

systemic velocity is V_{sys}. Plotting $\mathcal{V}$ against $\mathcal{X}$ then gives a straight line with slope $\Omega_p \sin i$. With this approach, the problem of centring errors becomes one of fixing an arbitrary reference position and velocity frame common to all the slits, which in general is much easier to achieve.

(ii) *Small signal-to-noise ratios.* $\mathcal{V}$ and $\mathcal{X}$ measure differences across $X = 0$ and are, therefore, susceptible to noise. This is particularly true for $\mathcal{V}$, for which the non-axisymmetric part of V_{los} is not much larger than typical measurement errors. Merrifield & Kuijken (1995) overcame this problem by projecting their slit spectra along the spatial direction thereby increasing the signal-to-noise ratio of $\mathcal{V}$ significantly. This projection amounts to carrying out the required velocity integral directly in photon space. The signal in $\mathcal{X}$ is typically much better constrained, since bars tend to be bright.

(iii) *Sensitivity to errors in the position angle of the disc.* This was first recognized by Debattista & Williams (in preparation). They used two-dimensional Fabry–Perot absorption-line spectroscopy of NGC 7079 to show that small errors in the derived position angle (PA) of the disc translate into large errors in Ω_p. For example, for NGC 7079, they found that an error of as little as 5° in the disc PA would result in an error of 100 per cent in Ω_p. As the
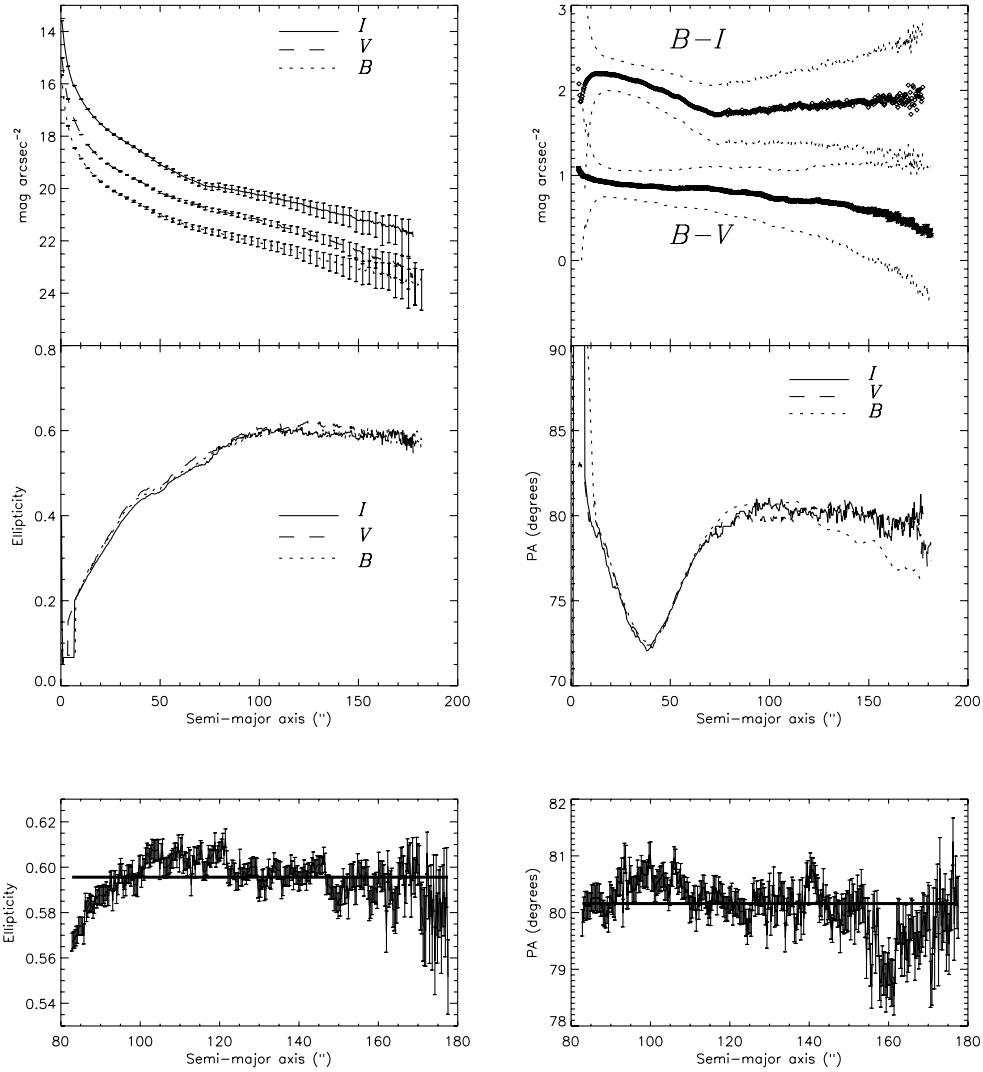
Figure 2. Surface brightness (top left), colour (top right), ellipticity (centre left) and PA (centre right) radial profiles of the ellipse fits to the isophotes of NGC 1023. The full, dotted and dashed lines show results for *I*, *V* and *B* bands respectively. The bottom two panels show the *I*-band ellipticity (left) and PA (right) for $R \gtrsim 80$ arcsec, which we averaged to determine the inclination and PA of the disc. The solid lines represent the average values in the range $\epsilon = 0.595$ (corresponding to $i = 66°.4$) and PA = $80°.2$.

uncertainties in published values of PA for disc galaxies are often at the 5° level, each application of the TW method requires careful measurement of the disc PA. Highly inclined galaxies and galaxies in which the bar is at about 45° to the disc major axis, are less sensitive to errors in disc PA. We note that past applications of the TW method using slits have been to well studied galaxies (Merrifield & Kuijken 1995; Gerssen et al. 1999), so that it is very unlikely that large errors of this type were introduced.

In this work, we have followed the prescriptions of Merrifield & Kuijken (1995) to deal with the centring and signal-to-noise ratio problems. We dealt with the sensitivity to errors in disc PA by obtaining deep surface photometry of NGC 1023 in advance of the spectroscopy.

3 GLOBAL PROPERTIES OF NGC 1023

NGC 1023 (UGC 2154) is a highly inclined lenticular galaxy classified as SB0 by Nilson (1973), as $SB0_1(5)$ by Sandage & Tammann (1981), and as $SB0^-$(rs) by de Vaucouleurs et al. (1991, hereafter RC3). Its total *B*-band magnitude is $B_T = 10.35$ (RC3),

which, after correcting for inclination and extinction, corresponds to $M_{B_T}^0 = -19.96$ for an adopted distance of 10.2 Mpc (Faber et al. 1997; $H_0 = 80 \, \mathrm{km \, s^{-1} \, Mpc^{-1}}$).

NGC 1023 is the brightest member of the LGG 70 group (Garcia 1993). Its closest companion, designated NGC 1023A by Hart, Davies & Johnson (1980), is a low-luminosity condensation located near the eastern end of the major axis. The centres of the two objects are separated by an angular distance of 2.7 arcmin (RC3), corresponding to a projected linear distance of about 8 kpc at 10.2 Mpc. The proximity of NGC 1023A to NGC 1023 led Arp (1966) to include NGC 1023 in the section of his Atlas of Peculiar Galaxies (Plate 135) devoted to E-like galaxies with nearby fragments. NGC 1023A was recognized as an individual galaxy by Barbon & Capaccioli (1975) and classified as Magellanic irregular or late-type dwarf galaxy by Capaccioli, Lorenz & Afanasiev (1986). High resolution radio observations by Sancisi et al. (1984) found a complex structure and kinematics for the neutral hydrogen. Most of it was shown to be outside the galaxy and consists of tails and bridges connecting NGC 1023 to three companions, including NGC 1023A. This morphology suggests an interaction with NGC
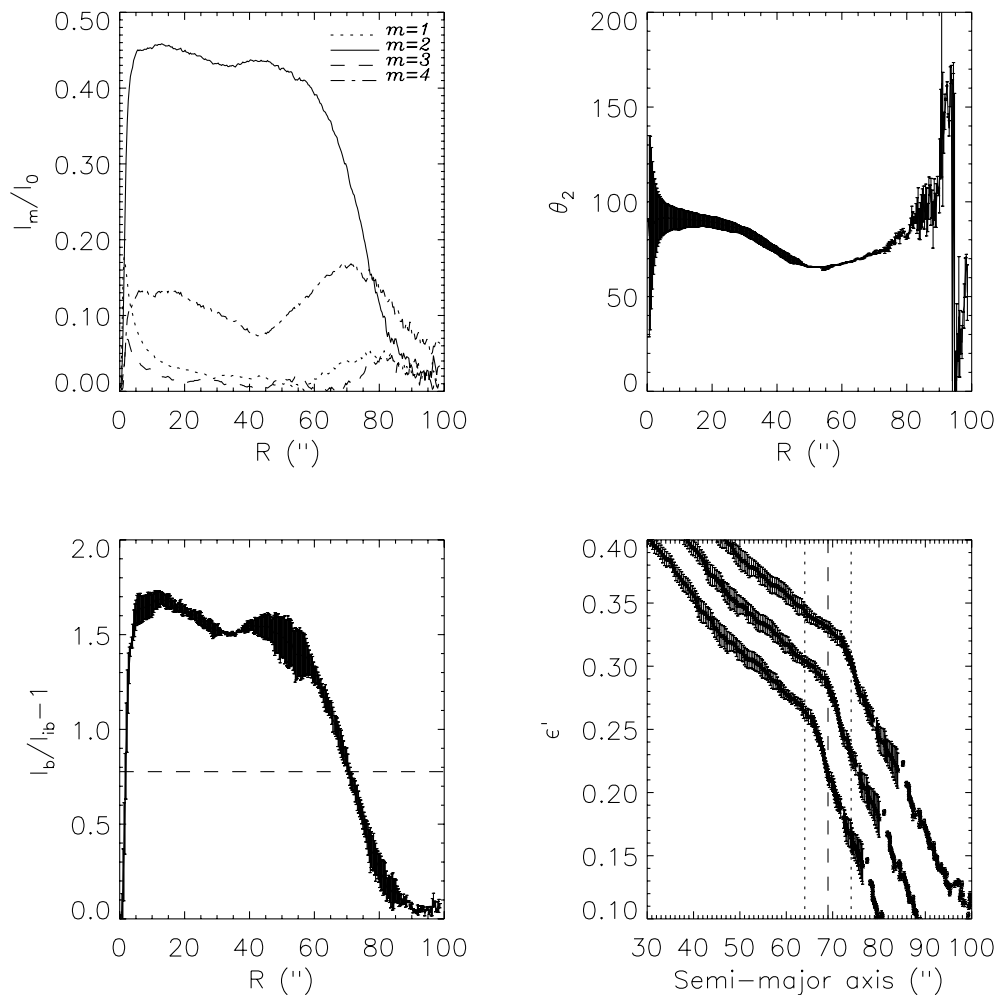
Figure 3. Fourier analysis of the deprojected *I*-band light distribution of NGC 1023. The top left panel shows the relative amplitudes of the $m = 1$ to $m = 4$ Fourier components, which reveals that $m = 2$ dominates. The top right panel shows the phase angle of the $m = 2$ Fourier component; inside $R \simeq 30$ arcsec, the system is clearly dominated by the spheroidal bulge, which deprojects into a feature along the minor axis. In the range 50 arcsec $\lesssim R \lesssim 70$ arcsec, θ_2 reaches a minimum of $\sim 65°$, but is not constant anywhere. The panel on the bottom left shows the bar/interbar intensity ratio. The dashed line indicates half of the peak intensity (excluding the peak at $R < 30$ arcsec since this is an artefact of the bulge deprojection). The bottom right panel shows an alternative measure of a_B, based on the deprojected ellipticities, ϵ'; the sharp break in ϵ' at semi-major axis $\simeq 69$ arcsec (indicated by the vertical dashed line) is identified as a_B. In this panel, the upper, central and lower set of points correspond to a deprojection assuming $i = 65°.2$, $66°.4$ and $67°.6$ respectively.

1023A, a conclusion also reached by Capaccioli et al. (1986). Although it is rich in neutral hydrogen, NGC 1023 is undetected in ionized (Pogge & Eskridge 1993; Sánchez-Portal et al. 2000) and molecular gas (Sofue et al. 1993; Taniguchi et al. 1994), making application of the TW method to it possible.

Surface photometry of NGC 1023 has been obtained in several optical (e.g. Barbon & Capaccioli 1975; Kormendy 1985; Lauer et al. 1995; Sánchez-Portal et al. 2000; Bower et al. 2001) and near-infrared bands (Möllenhoff & Heidt 2001). Detailed stellar kinematics have been measured by Simien & Prugniel (1997, PA = 87°, 177°), Neistein et al. (1999, PA = 87°), and recently by Bower et al. (2001, PA = 0°, 45°, 90°), who inferred the presence of a supermassive black hole of $4 \times 10^7 \, M_\odot$ by three-integral, axisymmetric modelling. Sil'chenko (1999) observed the circum-nuclear region of NGC 1023 via two-dimensional spectroscopy, disentangling a kinematically and chemically decoupled stellar disc (with a radius of 80 pc). The stars of this nuclear disc have a mean age of 7 Gyr and are substantially younger than the rest of the galaxy, which is characterized by extremely red integrated colours (RC3) and without global star formation (Pogge & Eskridge 1993).

4   SURFACE PHOTOMETRY AND DATA REDUCTION

4.1   Observations and reduction

We observed NGC 1023 during 2000 December 27–28 at the 1-m Jacobus Kapteyn Telescope (JKT) located at the Roque de los Muchachos Observatory (ORM), La Palma. The detector consisted of a SITe2 device, with 2048×2048 pixels and an image scale of 0.33 arcsec pixel^{-1}, giving an unvignetted field of view of about 10×10 arcmin^2. The seeing during the observing run varied from 1 to 1.5 arcsec. Table 1 gives the log of the photometric observations. The galaxy was imaged using the Harris *B*, *V* and *I* bandpasses. Deep observations were taken in all filters, reaching $\mu_I \simeq 22$ mag arcsec^{-2} and $\mu_B \simeq 24$ mag arcsec^{-2}.

The images were reduced using standard IRAF[1] tasks. A run of 10 bias images was obtained each night, which were combined into

---

Fig. 1 shows the reduced image of the galaxy in the *B* band and the *B − I* colour map image.

4.2 Isophotal analysis and bar length

We analysed the isophotal profiles of the galaxy by masking NGC 1023A and the foreground stars, then fitting ellipses using the IRAF task ELLIPSE. We first allowed the centres of the ellipses to vary, to test whether the optical disc is disturbed. Within the errors of the fits, we found no evidence of a varying centre. Thus the inner disc of NGC 1023 has had enough time to settle if it had been disturbed in the tidal interaction suggested by the H I. The ellipse fits were therefore repeated with the ellipse centres fixed; the resulting azimuthally averaged surface brightness, *B − I* colour, ellipticity and PA profiles are plotted in Fig. 2. These are in good agreement with the surface photometry of Sánchez-Portal et al. (2000), although our surface photometry reaches fainter surface brightness. The PA and ellipticity profiles are similar for all bandpasses, suggesting that there is little, or uniform, obscuration, as required for the TW method. Furthermore, at large radii, the *B − I* profile (see Fig. 2) is flat, which is further evidence of little obscuration. The only structure seen in the *B − I* profile is a small gradient in the region where the bulge and bar dominate. This gradient is in the sense of a bulge redder than the disc, which is most likely caused by an age difference between the bulge and disc stellar populations. There is also a small colour gradient in the bar region, but the colour variation is not patchy and is therefore unlikely to be caused by dust. We fitted the PA and inclination of the disc by averaging the *I*-band data at semi-major axis greater than 80 arcsec, finding PA = $80°.2 ± 0°.5$ and $i = 66°.4 ± 1°.2$. Application of the TW method generally requires a PA measured to ~5° accuracy (Debattista & Williams, in preparation); we note that the value of the PA given in the RC3 is 87°. Our value of the PA is in very good agreement with that measured by Möllenhoff & Heidt (2001), who found PA = $79°.15$ in the *J* band, $80°.42$ in the *H* band, and $78°.84$ in the *K* band, for an average of $79°.5 ± 0°.7$.

We measured the disc exponential scalelength, R_d, from our *I*-band surface photometry in the region outside the bar ($R \gtrsim 80$ arcsec). We obtained $R_d = 59$ arcsec, corresponding to 2.9 kpc at our assumed distance.

The most natural way to measure a_B is with a Fourier analysis of the azimuthal luminosity profile (Ohta, Masaru & Wakamatsu 1990; Aguerri et al. 2000), which we have applied here. We began by deprojecting the *I*-band image of the galaxy by a flux-conserving stretch along the minor axis by the factor $1/\cos i$. NGC 1023 contains a significant spheroidal bulge: the bulge-disc model decompositions of Möllenhoff & Heidt (2001) for this galaxy have a bulge that accounts for about 30 per cent to 50 per cent of the near-infrared light. Since we have not attempted to subtract the bulge, we expect that, in deprojection, it appears as a structure elongated with the minor axis, dominating the centre of the galaxy. We then decomposed the deprojected luminosity profile, $I(R, \phi)$, where (R, ϕ) are plane polar coordinates in the galaxy frame, into a Fourier series:

$$I(R, \phi) = \frac{A_0(R)}{2} + \sum_{m=1}^{\infty} [A_m(R) \cos(m\phi) + B_m(R) \sin(m\phi)] \quad (3)$$

where the coefficients are defined by

$$A_m(R) = \frac{1}{\pi} \int_0^{2\pi} I(R, \phi) \cos(m\phi) \, d\phi \quad (4)$$

Figure 4. Best-fitting ellipses to the *I*-band isophotes (a) before and (b) after deprojection to the NGC 1023 disc plane ($i = 66°.4$ and PA = $80°.2$). The system has been rotated so that the disc major axis is horizontal. Bold-line ellipses have deprojected semi-major axes of 60, 70 and 80 arcsec; the straight lines indicate the major axes of these three ellipses.

a single bias frame and subtracted from the object frames. The images were flat-fielded using sky flats taken in all filters at the beginning and end of each observing night. The sky background level was removed by fitting a second-order polynomial to the regions free of sources in the images.

For the photometric calibration of the galaxies, standard stars of known magnitudes were observed. The calibration constant includes corrections for atmospheric and Galactic extinction, and a colour term. No attempt was made to correct for internal extinction. The atmospheric extinction was taken from the differential aerosol extinction for the ORM (King 1985). The Galactic extinction in the *B* band was taken from Schlegel, Finkbeiner & Davis (1998). We used the Galactic extinction law from Cardelli, Clayton & Mathis (1989) in order to get the extinction in the other filters.

Table 2. Stellar kinematics of NGC 1023. These data are plotted in Fig. 5.

Major Axis

r [″]	v [km s⁻¹]	σ [km s⁻¹]	h3	h4
−108.76	852.3 ± 42.5	95.8 ± 27.9	−0.090 ± 0.232	−0.365 ± 0.200
−82.56	834.8 ± 28.5	98.1 ± 19.2	−0.109 ± 0.200	−0.171 ± 0.271
−59.33	791.9 ± 24.5	114.1 ± 20.2	−0.040 ± 0.194	−0.060 ± 0.103
−45.82	808.1 ± 18.5	107.3 ± 15.4	−0.091 ± 0.150	−0.085 ± 0.118
−36.62	783.6 ± 16.4	123.6 ± 13.2	−0.040 ± 0.151	−0.053 ± 0.123
−29.99	738.7 ± 19.4	154.1 ± 16.2	−0.063 ± 0.112	−0.072 ± 0.127
−24.93	725.0 ± 15.7	168.3 ± 15.2	0.046 ± 0.078	−0.082 ± 0.099
−20.98	720.3 ± 17.7	164.9 ± 18.3	−0.019 ± 0.066	−0.003 ± 0.104
−17.83	717.0 ± 17.0	164.8 ± 14.6	−0.023 ± 0.086	−0.104 ± 0.114
−15.37	716.4 ± 13.7	166.8 ± 14.1	0.047 ± 0.064	−0.057 ± 0.087
−13.32	717.4 ± 14.4	168.9 ± 16.1	0.028 ± 0.059	−0.012 ± 0.086
−11.53	713.1 ± 13.1	160.8 ± 12.9	−0.041 ± 0.057	−0.025 ± 0.083
−10.02	703.1 ± 12.4	191.4 ± 12.3	0.014 ± 0.043	−0.029 ± 0.048
−8.79	685.3 ± 12.2	192.1 ± 10.5	0.007 ± 0.043	−0.071 ± 0.051
−7.69	693.1 ± 13.9	189.1 ± 14.0	0.002 ± 0.048	−0.030 ± 0.056
−6.74	695.1 ± 12.2	191.3 ± 11.7	−0.010 ± 0.041	−0.024 ± 0.045
−5.91	691.8 ± 11.0	173.2 ± 12.2	−0.019 ± 0.043	−0.001 ± 0.058
−5.08	668.9 ± 12.9	191.4 ± 12.8	−0.024 ± 0.043	−0.017 ± 0.048
−4.40	670.7 ± 13.0	181.4 ± 14.9	0.013 ± 0.047	0.004 ± 0.059
−3.85	660.2 ± 12.6	200.7 ± 12.1	−0.005 ± 0.042	−0.022 ± 0.042
−3.30	665.0 ± 10.6	200.2 ± 9.9	−0.032 ± 0.035	−0.013 ± 0.035
−2.75	669.6 ± 11.5	196.0 ± 10.3	−0.022 ± 0.039	−0.036 ± 0.040
−2.34	681.8 ± 12.7	194.3 ± 12.9	−0.028 ± 0.041	−0.003 ± 0.045
−2.07	674.1 ± 11.3	198.6 ± 12.5	0.004 ± 0.037	0.019 ± 0.041
−1.79	672.3 ± 11.8	199.6 ± 11.1	−0.040 ± 0.039	−0.019 ± 0.039
−1.52	674.0 ± 10.3	203.1 ± 10.7	−0.030 ± 0.033	0.017 ± 0.035
−1.24	683.3 ± 11.3	208.2 ± 10.2	−0.027 ± 0.038	−0.029 ± 0.035
−0.97	681.2 ± 11.2	202.6 ± 10.5	−0.030 ± 0.037	−0.016 ± 0.036
−0.69	661.3 ± 12.2	224.3 ± 11.1	−0.008 ± 0.042	−0.029 ± 0.037
−0.42	648.1 ± 10.5	216.1 ± 10.5	−0.024 ± 0.034	0.005 ± 0.033
−0.14	615.9 ± 23.2	247.0 ± 32.0	0.020 ± 0.131	0.041 ± 0.113
0.13	609.5 ± 25.3	236.3 ± 29.6	0.064 ± 0.100	−0.002 ± 0.076
0.41	558.6 ± 9.2	215.1 ± 10.2	0.124 ± 0.031	−0.002 ± 0.036
0.68	550.7 ± 9.4	215.5 ± 9.7	0.082 ± 0.032	−0.001 ± 0.033
0.96	534.0 ± 10.6	211.9 ± 10.7	0.062 ± 0.037	−0.011 ± 0.037
1.23	532.8 ± 10.1	200.7 ± 10.8	0.066 ± 0.036	−0.011 ± 0.040
1.51	536.2 ± 10.1	205.6 ± 11.3	0.083 ± 0.035	0.003 ± 0.039
1.78	527.2 ± 11.7	211.4 ± 10.9	0.019 ± 0.040	−0.028 ± 0.038
2.06	527.3 ± 15.7	211.5 ± 16.4	0.020 ± 0.053	−0.006 ± 0.052
2.33	529.1 ± 12.2	213.2 ± 12.0	0.052 ± 0.042	−0.012 ± 0.040
2.61	534.5 ± 13.6	206.3 ± 16.4	0.116 ± 0.048	0.019 ± 0.056
3.01	552.2 ± 12.0	207.6 ± 15.6	0.097 ± 0.039	0.066 ± 0.048
3.56	550.0 ± 11.7	210.8 ± 12.0	0.040 ± 0.040	−0.004 ± 0.040
4.11	549.5 ± 11.3	211.7 ± 11.4	0.058 ± 0.039	−0.009 ± 0.039
4.66	533.6 ± 11.7	194.4 ± 13.4	0.046 ± 0.041	0.009 ± 0.047
5.35	538.3 ± 9.0	196.4 ± 10.7	0.111 ± 0.036	−0.038 ± 0.045
6.17	531.4 ± 13.4	204.0 ± 14.8	−0.017 ± 0.043	0.017 ± 0.046
25.89	497.4 ± 16.8	164.7 ± 18.2	0.068 ± 0.091	−0.044 ± 0.106
31.20	475.4 ± 18.1	137.7 ± 15.5	0.063 ± 0.136	−0.072 ± 0.128
38.25	438.6 ± 15.5	115.9 ± 11.8	0.082 ± 0.127	−0.067 ± 0.107
48.38	430.4 ± 11.4	82.4 ± 9.9	−0.020 ± 0.105	−0.073 ± 0.071
64.33	403.5 ± 19.9	85.2 ± 13.6	0.119 ± 0.165	−0.148 ± 0.130
89.29	407.5 ± 28.0	92.6 ± 19.0	0.148 ± 0.199	−0.161 ± 0.327
112.90	392.2 ± 45.5	84.7 ± 30.8	0.311 ± 0.277	−0.172 ± 0.356

12″ North Offset

r [″]	v [km s⁻¹]	σ [km s⁻¹]	h3	h4
−78.35	814.6 ± 41.8	121.2 ± 50.2	−0.057 ± 0.233	−0.073 ± 0.231
−56.44	809.1 ± 32.8	109.5 ± 28.5	0.024 ± 0.211	−0.107 ± 0.170
−43.07	760.6 ± 30.4	111.4 ± 22.5	−0.109 ± 0.217	−0.107 ± 0.145
−34.80	743.5 ± 28.5	126.2 ± 18.8	0.046 ± 0.140	−0.097 ± 0.194
−28.68	714.1 ± 27.6	125.0 ± 17.1	0.020 ± 0.137	−0.162 ± 0.194
−23.61	709.2 ± 27.1	118.7 ± 21.7	−0.014 ± 0.168	−0.079 ± 0.206
−19.23	669.9 ± 23.6	154.7 ± 17.6	0.078 ± 0.122	−0.126 ± 0.145
−15.39	682.0 ± 17.3	146.6 ± 14.3	0.019 ± 0.088	−0.100 ± 0.129
−12.11	653.2 ± 15.9	143.7 ± 13.6	0.010 ± 0.081	−0.078 ± 0.119
−9.22	650.4 ± 19.0	149.4 ± 16.8	−0.015 ± 0.086	−0.047 ± 0.118
−6.49	636.1 ± 17.5	171.1 ± 17.5	0.081 ± 0.078	−0.032 ± 0.084
−3.88	626.6 ± 17.8	186.2 ± 19.7	0.003 ± 0.066	0.000 ± 0.074
−1.40	602.2 ± 14.5	176.6 ± 14.3	0.033 ± 0.057	−0.028 ± 0.069
1.07	592.4 ± 14.7	159.9 ± 13.8	0.036 ± 0.064	−0.034 ± 0.081
3.53	585.8 ± 16.9	167.8 ± 17.3	0.029 ± 0.069	−0.018 ± 0.083
6.13	539.7 ± 16.3	177.7 ± 15.6	0.069 ± 0.067	−0.056 ± 0.080
9.02	522.3 ± 19.0	152.1 ± 17.1	−0.063 ± 0.085	−0.043 ± 0.112
12.29	542.2 ± 15.9	162.3 ± 16.6	0.036 ± 0.067	0.004 ± 0.082
16.12	547.4 ± 18.2	176.4 ± 18.7	0.036 ± 0.071	−0.030 ± 0.084
20.76	507.8 ± 21.4	131.6 ± 14.1	0.046 ± 0.141	−0.122 ± 0.154
26.72	483.6 ± 29.1	138.1 ± 20.0	0.048 ± 0.136	−0.122 ± 0.162
34.99	446.8 ± 24.0	99.0 ± 14.0	0.058 ± 0.213	−0.191 ± 0.132
47.61	416.4 ± 57.6	117.4 ± 46.8	0.158 ± 0.236	−0.122 ± 0.192
66.86	414.1 ± 27.1	68.4 ± 20.1	−0.058 ± 0.255	−0.161 ± 0.119
96.37	424.1 ± 32.3	55.7 ± 31.0	0.001 ± 0.230	−0.167 ± 0.165

16″ South Offset

r [″]	v [km s⁻¹]	σ [km s⁻¹]	h3	h4
−96.43	834.8 ± 38.4	79.1 ± 25.4	−0.075 ± 0.250	−0.270 ± 0.179
−75.58	800.9 ± 37.1	77.9 ± 21.6	0.006 ± 0.199	−0.311 ± 0.223
−53.66	793.2 ± 29.8	94.7 ± 26.1	−0.029 ± 0.206	−0.079 ± 0.140
−38.07	779.7 ± 28.9	88.7 ± 18.8	0.029 ± 0.224	−0.109 ± 0.128
−28.42	786.6 ± 28.3	100.5 ± 16.7	0.020 ± 0.218	−0.107 ± 0.112
−21.04	711.6 ± 30.2	152.8 ± 27.2	−0.053 ± 0.178	−0.086 ± 0.135
−15.18	704.1 ± 28.8	134.2 ± 27.2	−0.052 ± 0.186	0.009 ± 0.128
−10.40	647.1 ± 27.0	154.9 ± 21.1	−0.094 ± 0.184	−0.152 ± 0.145
−6.15	654.5 ± 21.9	145.5 ± 20.2	−0.029 ± 0.140	−0.040 ± 0.132
−2.18	633.8 ± 30.8	164.8 ± 24.3	−0.104 ± 0.158	−0.134 ± 0.162
1.52	606.4 ± 23.7	163.1 ± 18.2	0.150 ± 0.131	−0.186 ± 0.154
5.23	594.6 ± 18.0	140.3 ± 16.0	−0.056 ± 0.140	−0.057 ± 0.113

Table 2 – *continued*

r [']	v [km s^{-1}]	σ [km s^{-1}]	h$_3$	h$_4$	r [']	v [km s^{-1}]	σ [km s^{-1}]	h$_3$	h$_4$
7.00	534.5 ± 12.6	191.2 ± 12.8	0.013 ± 0.043	−0.022 ± 0.049	9.06	594.3 ± 24.9	162.5 ± 24.2	−0.001 ± 0.101	−0.039 ± 0.144
7.95	537.8 ± 14.2	189.2 ± 14.5	−0.024 ± 0.048	−0.021 ± 0.056	13.05	591.2 ± 21.2	150.5 ± 19.5	0.020 ± 0.133	−0.064 ± 0.142
9.06	525.0 ± 14.3	203.0 ± 13.4	0.006 ± 0.048	−0.035 ± 0.047	17.43	548.2 ± 25.6	133.7 ± 21.7	0.017 ± 0.189	−0.064 ± 0.127
10.29	518.0 ± 13.7	188.2 ± 14.9	0.007 ± 0.047	−0.012 ± 0.056	22.37	516.1 ± 23.3	128.5 ± 19.2	0.072 ± 0.164	−0.064 ± 0.128
11.80	533.2 ± 13.9	186.6 ± 15.0	0.043 ± 0.051	−0.034 ± 0.063	27.83	511.8 ± 24.2	129.7 ± 19.3	0.061 ± 0.177	−0.096 ± 0.134
13.58	559.2 ± 12.8	186.9 ± 13.4	0.103 ± 0.055	−0.087 ± 0.072	34.42	489.1 ± 37.7	141.7 ± 34.6	0.296 ± 0.191	0.040 ± 0.204
15.77	531.0 ± 14.1	173.2 ± 16.3	−0.004 ± 0.053	0.014 ± 0.075	43.89	458.7 ± 35.7	108.3 ± 27.8	0.135 ± 0.250	−0.075 ± 0.147
18.50	509.1 ± 15.1	160.1 ± 14.4	0.013 ± 0.076	−0.071 ± 0.104	59.92	438.6 ± 36.8	85.1 ± 25.3	−0.001 ± 0.198	−0.184 ± 0.179
21.79	502.6 ± 17.8	151.0 ± 16.8	0.123 ± 0.113	−0.053 ± 0.106	86.58	489.2 ± 50.1	89.8 ± 44.6	0.183 ± 0.212	−0.124 ± 0.235

and

$$B_m(R) = \frac{1}{\pi} \int_0^{2\pi} I(R, \phi) \sin(m\phi) \, d\phi. \tag{5}$$

The Fourier amplitude of the *m*th component is defined as

$$I_m(R) = \begin{cases} A_0(R)/2, & m = 0, \\ \sqrt{A_m^2(R) + B_m^2(R)}, & m \neq 0. \end{cases} \tag{6}$$

Fig. 3 shows the first ($m = 1, 2, 3, 4$) relative Fourier amplitudes, I_m/I_0, of the *I*-band image as a function of *R*. The bar is evidenced by a strong $m = 2$ component. Fig. 3 also shows the bar/interbar intensity as a function of *R*. The bar intensity, I_b, is defined as the sum of the even Fourier components, $I_0 + I_2$, while the interbar intensity, I_{ib}, is given by $I_0 - I_2$ (Ohta et al. 1990; Elmegreen & Elmegreen 1990; Aguerri et al. 2000). Ohta et al. (1990) arbitrarily defined a_B as the outer radius for which $I_b/I_{ib} = 2$; as Aguerri et al. (2000) pointed out, a fixed value of I_b/I_{ib} cannot account for the wide variety of bar luminosities present in galaxies. Instead, Aguerri et al. (2000) defined a_B as the full width at half maximum (FWHM) of the curve of I_b/I_{ib}. Using this definition, but excluding the peak in I_b/I_{ib} resulting from the deprojected bulge, we obtain $a_B = 69 \pm 5$ arcsec. The phase angle, $\theta_2(R) = \tan^{-1}[A_2(R)/B_2(R)]$, of the $m = 2$ component is shown in Fig. 3. The bulge dominates in the inner 20 arcsec (with $\theta_2 \approx 90°$, as expected), with a transition from bulge to bar occurring in the range $20 \text{ arcsec} \lesssim R \lesssim 50 \text{ arcsec}$. In the region $50 \text{ arcsec} \lesssim R \lesssim 70 \text{ arcsec}$, θ_2 has a minimum, implying the bar extends to somewhere here. However, θ_2 is not constant, because of the influence of the bulge and the disc, and it cannot be used to determine a_B.

A independent measure of a_B was obtained by deprojecting the ellipses which best fit the isophotes, averaging over the three bands, and examining the deprojected ellipticity, ϵ', as shown in Fig. 3. We find a sharp break in the slope of ϵ' at 69 ± 3 arcsec, which we identify as the end of the bar. We repeated this experiment, deprojecting with different *i* and PA within the standard errors of these quantities. The errors in PA do not significantly change the semi-major axis at which the break occurs, while those in *i* lead to changes in the break semi-major axis of ∼3 arcsec. Thus, our second estimate of $a_B = 69 \pm 4$ arcsec. Fig. 4 plots the projected and deprojected ellipses, from which the change at semi-major axis ∼70 arcsec can be discerned.

Outside the inner 5 arcsec, the largest twist arising from the bar of the isophotes away from the sky-plane major axis is only ≃8°, which occurs at 40 arcsec. We measured the bar's intrinsic angle from the major axis, ψ_{bar}, in the radial range 55 to 70 arcsec, averaged over the three bands. Owing to the contamination from the bulge, the deprojected isophotal ellipses are not constant in this range, so we used as the uncertainty in ψ_{bar} the largest deviation from the average. Thus we obtained $\psi_{bar} = 102 \pm 2°$, so that the bar is only some 12° from the minor axis, as can be seen in Fig. 4. This bar orientation, together with the large inclination and strong bulge, tend to obstruct our view of the bar. In this sense, NGC 1023 is not an ideal candidate for the TW method, and the expected values of $\mathcal{V}$ and $\mathcal{X}$ are likely to be small, as we show in Section 6. For this combination of inclination and ψ_{bar}, Debattista (in preparation) suggests an accuracy of ∼2°.5 in PA is required for accurate measurement of Ω_p.
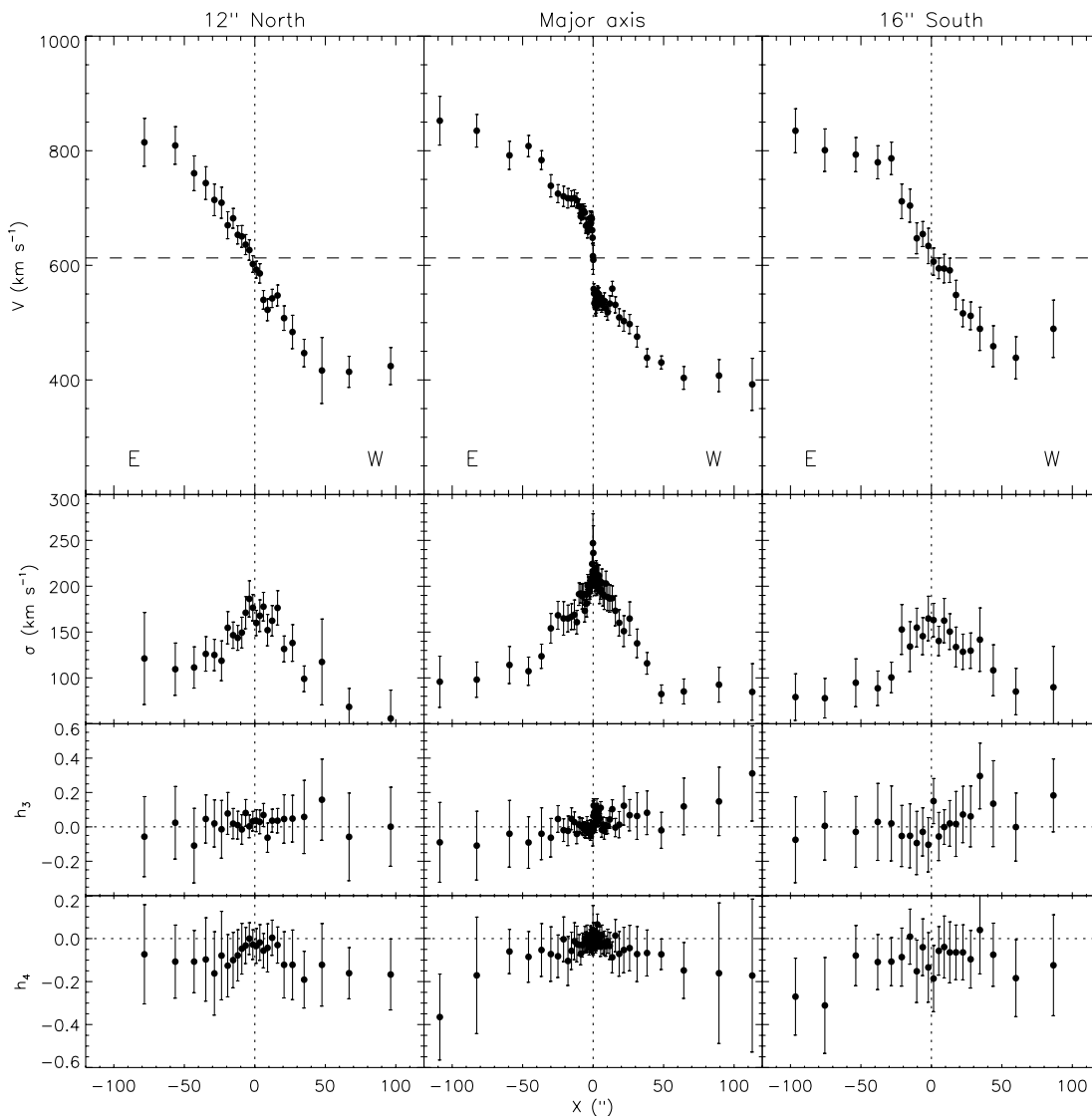
Figure 5. Stellar kinematics of NGC 1023. Each column shows the radial profiles of the four Gauss–Hermite moments (V, σ, h_3 and h_4) we measured along a given slit position. In the top panels the horizontal dashed line indicates the heliocentric systemic velocity of the NGC 1023. All velocities are plotted as observed, without correcting for the inclination. The full data are given in Table 2.

Table 3. The values of $\mathcal{V}$ and $\mathcal{X}$ for the three slits.

Offset	$\mathcal{X}$ (arcsec)	$\mathcal{V}$ (km s^{-1})
12 arcsec N	-1.82 ± 0.13	619.1 ± 5.4
Major axis	$+0.05 \pm 0.06$	614.5 ± 2.2
16 arcsec S	$+1.90 \pm 0.25$	603.7 ± 3.0

5   LONG-SLIT SPECTROSCOPY

5.1   Observations and data reduction

The spectroscopic observations of NGC 1023 were carried out at the ORM in La Palma, with the 3.6-m Telescopio Nazionale Galileo on 2001 February 1–2. The telescope mounted the Low Resolution Spectrograph (DOLORES). The HR-V grism No. 6 with 600 groove mm^{-1} was used in combination with the 0.7 arcsec × 8.1 arcmin slit and the thinned and back-illuminated

Loral CCD with 2048×2048 pixels of 15×15 μm^2. The wavelength range between 4697 and 6840 Å was covered with a reciprocal dispersion of 1.055 Å pixel^{-1}, which guarantees an adequate oversampling of the instrumental broadening function. Indeed, the instrumental resolution, obtained by measuring the width of emission lines of a comparison spectrum after the wavelength calibration, was 3.10 Å (FWHM). This corresponds to an instrumental dispersion $\sigma = 1.32$ Å (i.e. ~80 and ~60 km s^{-1} at the blue and red edges of the spectra, respectively). The angular sampling was 0.275 arcsec pixel^{-1}.

We obtained two 30-min spectra with the slit along the major axis (PA $= 80°$) and two offset spectra with the slit parallel to the major axis and shifted by 12 arcsec northward and 16 arcsec southward. The exposure time of each offset spectrum was 60 min. During the observing run, we took spectra of the giant stars HR 2035 (G8III), HR 2429 (K1III), HR 2503 (K4III), HR 2701 (K0III), and HR 5370 (K3III) to use as templates in measuring the stellar kinematics. At the beginning of each exposure, the slit was positioned by acquiring with DOLORES a series of target images. A spectrum of the comparison helium arc lamp was taken after
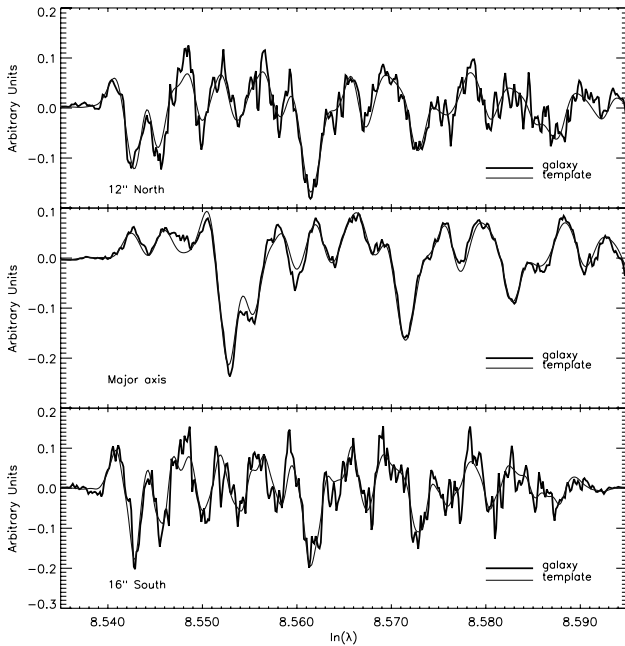
Figure 6. Galaxy spectra (thick lines), obtained by collapsing along the spatial direction, of the major axis and the two offset positions. They are compared with the template spectra (thin line) convolved with their corresponding LOSVDs. Galaxy and template spectra have been continuum-subtracted and tapered at the ends with a cosine bell function.

Table 4. Heliocentric systemic velocity based on optical measurements.

V_{sys} (km s^{-1})	Source
734 ± 41	Mayall & de Vaucouleurs (1962)
617 ± 19	Tonry & Davies (1981)
597 ± 9	Schechter (1983)
608 ± 9	Schechter (1983)
615 ± 20	Dressler & Sandage (1983)
620 ± 50	Capaccioli et al. (1986)
592 ± 15	Simien & Prugniel (1997)
606 ± 5	Weighted average of literature values
613 ± 3	This work

each target exposure to allow an accurate wavelength calibration. The value of the seeing FWHM during the galaxy exposures ranged between 0.7 and 1.0 arcsec as measured by fitting a two-dimensional Gaussian to the guide star.

All the spectra were bias-subtracted, flat-field corrected, cleaned of cosmic rays and wavelength-calibrated using standard MIDAS[2] routines. The bias level was determined from the bias frames obtained during the observing nights to check the CCD status. The flat-field correction was performed by means of both quartz lamp and twilight sky spectra, which were normalized and divided into all the spectra, to correct for pixel-to-pixel sensitivity variations and large-scale illumination patterns arising from slit vignetting. Cosmic rays were identified by comparing the counts in each pixel with the local mean and standard deviation (as obtained from

[2] MIDAS is developed and maintained by the European Southern Observatory.

Poisson statistics by taking into account the gain and read-out noise of the detector) and then corrected by interpolating over. The residual cosmic rays were corrected by manually editing the spectra. The wavelength calibration was performed by means of the MIDAS package XLONG. Each spectrum was rebinned using the wavelength solution obtained from the corresponding arc-lamp spectrum. We checked that the wavelength rebinning had been done properly by measuring the difference between the measured and predicted wavelengths (Osterbrock et al. 1996) for the brightest night-sky emission lines in the observed spectral range. The resulting accuracy in the wavelength calibration is ~ 1 km s^{-1}. The major-axis spectra were coadded using the centre of the stellar continuum as reference. In the resulting spectra, the contribution of the sky was determined by interpolating along the outermost 20 arcsec at the two edges of the slit, where the galaxy light was negligible, and then subtracted.

5.2 Stellar kinematics

We measured the stellar kinematics from the galaxy absorption features present in the wavelength range running from 4697–5570 Å and centred on the Mg line triplet ($\lambda\lambda$ 5164, 5173, 5184 Å). The spectra were rebinned along the spatial direction to obtain a nearly constant signal-to-noise ratio larger than 20 per resolution element (with a peak of 50 in the innermost regions of the major axis spectrum). At the outermost radii the signal-to-noise ratio decreases to ~ 10. The galaxy continuum was removed row-by-row by fitting a fourth to sixth order polynomial.

We used the Fourier Correlation Quotient method (FCQ, Bender 1990) following the prescriptions of Bender, Saglia & Gerhard (1994) and adopting HR 2035 as kinematical template. This allowed us to derive, for each spectrum, the line-of-sight velocity distribution (LOSVD) along the slit and to measure its moments, namely the radial velocity v, the velocity dispersion σ and the values of the coefficients h_3 and h_4. At each radius, they have been derived by fitting the LOSVD with a Gaussian plus third- and fourth-order Gauss–Hermite polynomials H_3 and H_4, which describe the asymmetric and symmetric deviations of the LOSVD from a pure Gaussian profile (van der Marel & Franx 1993; Gerhard 1993). We derived errors on the LOSVD moments from photon statistics and CCD read-out noise, calibrating them by Monte Carlo simulations as done by Bender et al. (1994) and Bower et al. (2001), who have recently derived the stellar kinematics of this galaxy along three axes (different from ours). In general, our errors are in the range of 10–20 km s^{-1} for v and σ, and 0.03–0.1 for h_3 and h_4, becoming larger for signal-to-noise ratios lower than 20. These errors do not take into account possible systematic effects arising from any template mismatch. The measured stellar kinematics along the major and the offset axes are reported in Table 2 and plotted in Fig. 5.

6   PATTERN SPEED

To compute the mean position of stars, $\mathcal{X}$, along the slits, we extracted profiles from the B, V and I-band surface photometry along the positions of the slits. The profiles in the V band (within which the wavelength range used in the spectroscopy falls) match very well the profiles obtained by collapsing the spectra along the wavelength direction, confirming that the slits were placed as intended. We used the broad-band profiles to compute $\mathcal{X}$ because these are less noisy than the spectral profiles, particularly at large radii. We therefore computed three values of $\mathcal{X}$ at each slit position,
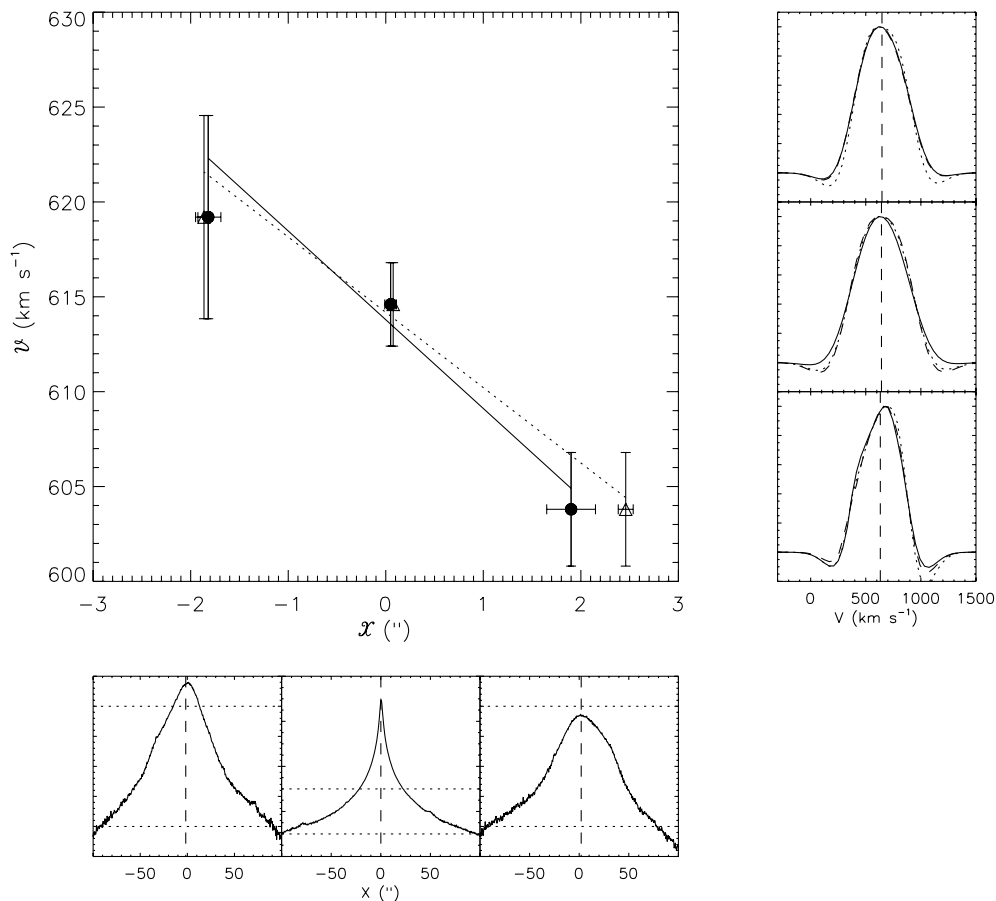
Figure 7. The pattern speed measurement for NGC 1023. The bottom three panels show the *V*-band profiles for the three slits (12 arcsec N, major axis and 16 arcsec S from left to right) with $\mathcal{X}$ indicated by the dashed vertical lines. The horizontal dotted lines indicate $\mu_V = 19\,\mathrm{mag\,arcsec^{-2}}$ and $\mu_V = 21\,\mathrm{mag\,arcsec^{-2}}$. The three panels on the right indicate the LOSVD for the three slits (12 arcsec N, major axis and 16 arcsec S from top to bottom), with $\mathcal{V}$ indicated by the dashed lines. The LOSVDs are constructed from the Gauss–Hermite moments; the three LOSVDs in each of these panels were obtained from different wavelength ranges (here, each is renormalized to the same maximum value, for clarity). The central panel plots $\mathcal{V}$ against $\mathcal{X}$ (solid circles); the slope of the best-fitting straight line (indicated by the solid line) is $\Omega_{\mathrm{p}} \sin i = 4.7 \pm 1.7\,\mathrm{km\,s^{-1}\,arcsec^{-1}}$. The open triangles and dotted line indicates the results for using just the *I* band to measure $\mathcal{X}$, which gives the largest values of $|\mathcal{X}|$ and therefore the smallest slope, $\Omega_{\mathrm{p}} \sin i = 4.0 \pm 1.4\,\mathrm{km\,s^{-1}\,arcsec^{-1}}$.

$\mathcal{X}_B$, $\mathcal{X}_V$ and $\mathcal{X}_I$. Each value of $\mathcal{X}$ was computed by Monte Carlo simulation, with photon, readout and sky noise to compute the errors. Another advantage to using the broad band surface photometry is that it allows us to test for contamination by NGC 1023A to the integrals. Formally, the integrals in equation 1 are over $-\infty \leq X \leq \infty$, but can be limited to $-X_{\max} \leq X \leq X_{\max}$ if $X_{\max}$ has reached the axisymmetric part of the disc; still larger values of $X_{\max}$ add noise only. In the case of NGC 1023, the presence of NGC 1023A introduces some additional light at negative X. The most severely contaminated slit is the one at 16 arcsec S, where $\mathcal{X}$ continues changing as ever larger values of $X_{\max}$ are used. We therefore found it useful to compare the 16 arcsec S profiles with the profiles at 16 arcsec N. For these latter profiles, there is no further signal to $\mathcal{X}$ beyond $X_{\max} = 60$ arcsec. The comparison also showed that there is little or no contamination to the 16 arcsec S slit inside $X_{\max} \sim 55$ arcsec. Furthermore, since NGC 1023A is quite blue, the contamination decreases in going from *B* to *V*, and especially to the *I* band. Therefore, to measure $\mathcal{X}$ at 16 arcsec S, we averaged the Monte Carlo results in the range 62 arcsec $\leq X_{\max} \leq 75$ arcsec (75 arcsec $\leq R \leq 85$ arcsec, where the disc is roughly axisymmetric) and then averaged over each band. In the remaining slits, contamination by NGC 1023A in the

major axis begins at $R \geq 100$ arcsec in all bands and is easily avoided, while the 12 arcsec N slit has no obvious contamination. We therefore also averaged them over 75 arcsec $\leq R \leq 85$ arcsec. Because of the colour gradient in the inner ~ 70 arcsec (Fig. 2), the value of $\mathcal{X}$ in the offset slits changes with the colour band used, with $|\mathcal{X}_I| > |\mathcal{X}_V| \gtrsim |\mathcal{X}_B|$. Therefore, by averaging over bands and then taking the largest discrepancy from the average as our error value, we are confident that we take into account any difference between the narrow wavelength range of the spectroscopy and the broad one of the surface photometry. The values thus obtained are given in Table 3.

If we have successfully avoided contamination by NGC 1023A, then we expect that, since NGC 1023 is nearly point-symmetric about its centre, the profile extracted from the surface photometry at Y should have a value of $\mathcal{X}$ roughly the negative of value for the profile extracted at -Y. For a profile extracted from the surface photometry at 16 arcsec N, we found $\mathcal{X} = -2.31 \pm 0.15$ arcsec averaged over the three bands, which is within 2σ of our value for $-\mathcal{X}$ at 16 arcsec S.

To measure the luminosity-weighted line-of-sight stellar velocity, $\mathcal{V}$, for each slit position, we collapsed each bidimensional spectrum along its spatial direction to obtain a one-dimensional
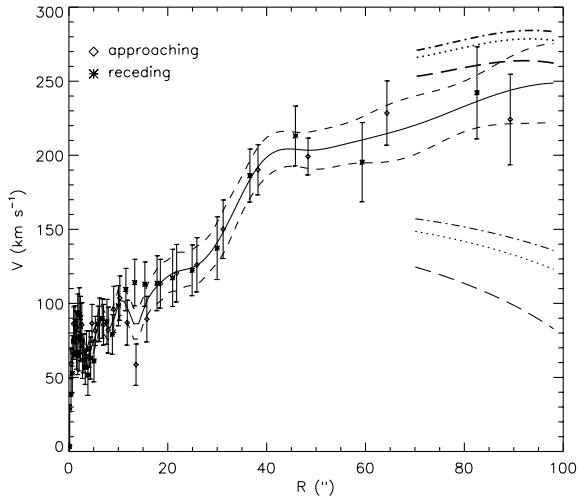
Figure 8. The stellar velocity streaming curve, V_* derived by subtracting V_{sys}, folding and deprojecting the observed velocities on the major axis. The data from the major axis are shown as diamonds (approaching side) and stars (receding side). The solid line and the dashed lines flanking it are our fitted spline together with the 1σ error interval. The asymmetric drift terms ($\sqrt{V_c^2 - V_*^2}$) are shown by the dot–dashed, dotted, and long-dashed lines ($\alpha = 0.0$, 0.5, and 1.0 respectively) in the lower right corner at $R \geq 70$ arcsec. The corresponding circular rotation curves, V_c, are shown in the bold lines.

Figure 9. The average value, a, (top panel) and the $\cos 2\phi$ component, b, (bottom panel) of the squared observed velocity dispersions. The top panel also indicates $a - b$. We fit straight lines to $a - b$ and b at $R \geq 70$ arcsec, as indicated.

spectrum. The resulting spectra have been analysed with the FCQ method using HR 2035 as template star. $\mathcal{V}$ is the radial velocity derived from the LOSVD of the one-dimensional spectra (see Fig. 6). For each slit position, the uncertainties on $\mathcal{V}$ were estimated by measuring it in different wavelength ranges between 4910 and 5560 Å (but always including the Mg triplet). The $\mathcal{V}$ values we derived along each slit are given in Table 3. We integrated the spectral rows at $X_{max} = 140$, 100 and 80 arcsec in the major-axis, northern and southern offset spectra, respectively. For the major-axis and northern offset spectra we were limited by the noise, which becomes dominant at larger radii ($S/N \leq 3$), while for the southern offset spectrum we decided to also try $X_{max} = 60$ arcsec, to check for contamination by NGC 1023A. We found that different choices of X_{max} do not affect our results for $\mathcal{V}$. The values of $\mathcal{V}$ we derived by integrating both offset spectra out to $X_{max} = 140$ arcsec (after removing by linear interpolation the contribution of foreground stars) are close to those in Table 3, although their errors increase by factors of 1.6 and 2 along the north and south slits, respectively. Therefore, within the errors obtained from the varying wavelength range, there is no evidence of contamination by NGC 1023A in $\mathcal{V}$ for the southern offset slit.

By performing our analysis with all the remaining template spectra, we found that $\mathcal{V}$ values are not affected by template mismatch (at least for our set of template stars). This is in agreement with the results of Bender et al. (1994) on the determination of the radial velocities with FCQ.

Using the data of Table 3, in Fig. 7 we plot $\mathcal{V}$ versus $\mathcal{X}$, fitting a straight line (using subroutine FITEXY in Numerical Recipes). The slope of this line is $\Omega_p \sin i = 4.7 \pm 1.7 \, \text{km s}^{-1} \, \text{arcsec}^{-1}$, which gives $\Omega_p = 5.1 \pm 1.8 \, \text{km s}^{-1} \, \text{arcsec}^{-1}$ (corresponding to $\Omega_p = 104 \pm 34 \, \text{km s}^{-1} \, \text{kpc}^{-1}$ at 10.2 Mpc). We have also fitted a 'slowest bar' line, using the values of $\mathcal{X}_l$ (which are largest, and therefore give the shallowest slope) for the 12 arcsec N and major-axis slits, and using $-\mathcal{X}_l$ from 16 arcsec N for the 16 arcsec S slit, as this has an even larger value of $|\mathcal{X}_l|$. The slope of this line, now ignoring
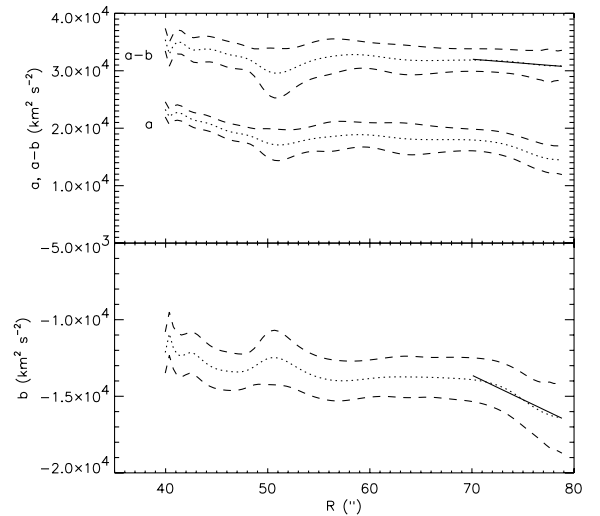
the uncertainties in $\mathcal{X}$, is $\Omega_p \sin i = 4.0 \pm 1.4 \, \text{km s}^{-1} \, \text{arcsec}^{-1}$ ($\Omega_p = 4.3 \pm 1.5 \, \text{km s}^{-1} \, \text{arcsec}^{-1}$).

To then determine $\mathcal{R}$, we need to measure D_L, which we approximate by the corotation radius, R_c, from the axisymmetric approximation. Debattista (1998) found that, for strong bars in N-body simulations, the approximation $D_L \simeq R_c$ involves an error of ~ 5 per cent. We therefore measured the rotation curve, $V_c(R)$, of NGC 1023. This is a two-step process: first we fitted tilted rings (with constant PA and inclination fixed to the value obtained from the surface photometry) to the data from all our slits, interpolating with cubic splines where necessary. This allowed us to measure the heliocentric systemic velocity, $V_{sys} = 613 \pm 3 \, \text{km s}^{-1}$, which is compared to the values based on optical data available in the literature in Table 4. By folding the major axis slit (which reaches furthest out in R) about the origin, after subtracting out V_{sys}, we obtained the stellar streaming velocities, $V_*(R)$, shown in Fig. 8.

We tested $V_*(R)$ by rotating it into the orientations of other slit observations available in the literature. The slits we compared with are those at PA $= 87°$ (Simien & Prugniel 1997; Neistein et al. 1999), PA $= 90°$ (Bower et al. 2001) and PA $= 177°$ (Simien & Prugniel 1997). Excluding the inner 2 arcsec, to avoid the effects of different seeing and/or slit widths, we find $\tilde{\chi}^2 \lesssim 1$ in all cases except for the PA $= 87°$ slit of Neistein et al. (1999), for which we obtained $\tilde{\chi}^2 = 2.5$ (for 27 points). Since the same PA is also covered by a slit from Simien & Prugniel (1997), which we match well ($\tilde{\chi}^2 = 0.8$ for 36 points), we conclude that the stellar streaming velocity profile we obtained is reasonable and in good agreement with previous data.

We then corrected for the asymmetric drift using the velocity dispersion data, to recover the true circular velocity, $V_c(R)$. Following equation (4–33) in Binney & Tremaine (1987), and assuming $\partial(\overline{v_R v_z})/\partial z \simeq 0$, we can write the asymmetric drift equation as

$$V_c^2 - V_*^2 = -\sigma_R^2 \left[\frac{\partial \ln \rho}{\partial \ln R} + \frac{\partial \ln \sigma_R^2}{\partial \ln R} + \left(1 - \frac{\sigma_\phi^2}{\sigma_R^2} \right) \right]. \quad (7)$$

The observed velocity dispersion, at a point (R, ϕ) in the galaxy

frame, is given by

$$\sigma_{\rm los}^2 = \tfrac{1}{2}\sin^2 i[(\sigma_R^2 + \sigma_\phi^2 + 2\sigma_z^2 \cot^2 i) - (\sigma_R^2 - \sigma_\phi^2)\cos 2\phi]$$

$$\equiv a(R, \phi) + b(R, \phi)\cos 2\phi. \tag{8}$$

where $\phi = 0$ is taken to be the major axis of the disc. When the disc is axisymmetric, a and b can only depend on R, in which case a and b are simply the first 2 even moments in a Fourier expansion of the line-of-sight velocity dispersion. For a disc with a flat rotation curve, $\sigma_\phi^2/\sigma_R^2 = 1/2$, which then allows us to obtain σ_R^2 from b. However, the profile of V_* we found for NGC 1023 is not obviously flat. (Furthermore, b is more sensitive to noisy data than is a.) In the general case, the asymmetric drift equation can be re-written in terms of both a and b, as follows:

$$V_{\rm c}^2 - V_*^2 = \frac{R}{\sin^2 i(1 + \alpha^2 \cot^2 i)} \left[\frac{a-b}{R_{\rm d}} - \frac{\partial}{\partial R}(a-b) \right] + \frac{2b}{\sin^2 i}, \tag{9}$$

where we have assumed that the disc density is exponential with scalelength $R_{\rm d}$ and $\alpha \equiv \sigma_z/\sigma_R$. Using the velocity dispersion data from our three slits and the near minor-axis data of Simien & Prugniel (1997), we measured $a - b$ and b. We fitted splines to interpolate between data points, and estimate errors from Monte Carlo simulation with Gaussian noise added from the error estimate on each point. The resulting profiles of a and b are shown in Fig. 9. Our procedure for measuring $V_*(R)$, a and b is valid only in the axisymmetric region outside the bar. Therefore we only apply the asymmetric drift correction to $R < 70$ arcsec; for this region, we fit straight lines to $a - b = -141\,(\pm61)R + 41884\,(\pm562)$ km^2 s^{-2} and to $b = -319\,(\pm39)R + 8706\,(\pm350)$ km^2 s^{-2}. With these values, we then correct the rotation curve, assuming $0.0 \le \alpha \le 1.0$. (This range of α is a reasonable one: in the Solar neighbourhood, Dehnen & Binney (1998) found $\alpha \simeq 0.54^{+0.02}_{-0.05}$, while in NGC 488, Gerssen, Kuijken & Merrifield (1997) measured $\alpha = 0.70 \pm 0.19$.) The resulting rotation curve is more or less flat, with $259 \lesssim V_{\rm c,flat} \lesssim 278$ km s^{-1}. Adding in quadrature a velocity uncertainty of 30 km s^{-1}, we obtain $V_{\rm c,flat} = 270 \pm 31$ km s^{-1}. (For comparison, Neistein et al. 1999 found $V_{\rm c} = 250 \pm 17$ km s^{-1}; we have checked that using a method similar to their equation (8) gives similar values for $V_{\rm c,flat}$ to those reported above.) If we extrapolate this value to smaller radii (which, at worst, overestimates $R_{\rm c}$ and, correspondingly, $\mathcal{R}$, unless the rotation curve is dropping over range 40 arcsec $\lesssim R \le 70$ arcsec, which seems unlikely from Fig. 8) we find $R_{\rm c} = V_{\rm c,flat}/\Omega_{\rm p} = 53 \pm 6^{+29}_{-14}$ arcsec, where the first error is due to the uncertainties in $V_{\rm c,flat}$ and the second error reflects uncertainties in $\Omega_{\rm p}$. We obtain, therefore, $\mathcal{R} = 0.77 \pm 0.10^{+0.42}_{-0.20}$ (where the first error now also includes the uncertainty in $a_{\rm B}$). For our 'slowest bar' estimate of the slope, we find $\mathcal{R} = 0.91 \pm 0.12^{+0.49}_{-0.23}$. We have found, therefore, that the bar in NGC 1023 is consistent with being a fast bar.

7 DISCUSSION AND CONCLUSIONS

We have found that the bar in NGC 1023 is fast, as are all bars which have been measured to date. Debattista & Sellwood (1998, 2000) showed that fast bars can persist only if the disc is maximal. Following Ostriker & Peebles (1973), it is sometimes thought that the unbarred (SA) galaxies are stabilized by massive DM haloes. However, massive DM haloes are not necessary for stabilizing

discs; a rapidly rising rotation curve in the inner disc, such as when a massive bulge is present, is also able to inhibit bar formation (Toomre 1981; Sellwood & Evans 2001). Debattista & Sellwood (1998) argued that unbarred HSB galaxies must also be maximal for, if HSB disc galaxies form a continuum of DM halo masses spanning massive DM halo-stabilized SA galaxies to maximal SB galaxies, then slow bars must also be found in the intermediate range of halo masses. If we seek to avoid intermediate halo masses and slow bars by postulating (for whatever reason) a bimodal DM halo mass distribution for HSB galaxies, then we are left with the possibility that tidal interactions can still form bars, which would be slow (Noguchi 1987; Salo 1991; Miwa & Noguchi 1998). Thus Debattista & Sellwood (2000) concluded that the absence of slow bars requires that all HSB disc galaxies are maximal. However, it is possible that no such slow bars have been found because of an observational bias against SB systems with evidence of tidal interactions.

We have chosen to study NGC 1023, in part, because it shows signs of a weak interaction in its past, without being at present significantly perturbed. The fast bar we found indicates that NGC 1023 has a maximal disc. If SA galaxies are stabilized by massive haloes, we should find slow bars in that fraction of SB galaxies in which the bar formed through the interaction. While it is not possible to reach a general conclusion on the DM content of SA galaxies based on our measurement for a single galaxy, a large enough sample of similar SB galaxies with mild interactions in the past will enable us to address this question.

REFERENCES

Aguerri J. A. L., Muñoz-Tuñón C., Varela A. M., Prieto M., 2000, A&A, 361, 841
Aguerri J. A. L., Hunter J. H., Prieto M., Varela A. M., Gottesman S. T., Muñoz-Tuñón C., 2001, A&A, 373, 786
Arp H., 1996, Atlas of Peculiar Galaxies. California Institute of Technology, Pasadena
Athanassoula E., 1992, MNRAS, 259, 345
Athanassoula E., 1996, in Buta R., Crocker D. A., Elmegreen B. G., eds,

ASP Conf. Ser. Vol. 91, IAU Colloq. 157, Barred Galaxies. Astron. Soc. Pac., San Francisco, p. 309

Barbon R., Capaccioli M., 1975, A&A, 42, 103

Bender R., 1990, A&A, 229, 441

Bender R., Saglia R. P., Gerhard O. E., 1994, MNRAS, 269, 785

Binney J., Tremaine S., 1987, Galactic Dynamics. Princeton Univ. Press, Princeton

Bower G. A. et al., 2001, ApJ, 550, 75

Capaccioli M., Lorenz H., Afanasjev V. L., 1986, A&A, 169, 54

Cardelli J. A., Clayton G. C., Mathis J. S., 1989, ApJ, 345, 245

Contopoulos G., 1980, A&A, 81, 198

Debattista V. P., 1998, PhD thesis, Rutgers University

Debattista V. P., Sellwood J. A., 1998, ApJ, 493, L5

Debattista V. P., Sellwood J. A., 2000, ApJ, 543, 704

Debattista V. P., Williams T. B., 2001, in Funes J. G., Corsini E. M., eds, ASP Conf. Ser. Vol. 230, Galaxy Disks and Disk Galaxies. Astron. Soc. Pac., San Francisco, p. 553

Dehnen W., Binney J. J., 1998, MNRAS, 298, 387

de Vaucouleurs G., de Vaucouleurs A., Corwin H. G., Buta R. J., Paturel G., Fouquè P., 1991, Third Reference Catalogue of Bright Galaxies. Springer-Verlag, New York (RC3)

Dressler A., Sandage A., 1983, ApJ, 265, 664

Elmegreen B., 1996, in Buta R., Crocker D. A., Elmegreen B. G., eds, ASP Conf. Ser. Vol. 91, IAU Colloq. Vol. 157, Barred Galaxies. Astron. Soc. Pac., San Francisco, p. 197

Elmegreen B. G., Elmegreen D. M., 1990, ApJ, 355, 52

England M. N., Gottesman S. T., Hunter J. H., 1990, ApJ, 348, 456

Eskridge P. B. et al., 2000, AJ, 119, 536

Faber S. M. et al., 1997, AJ, 114, 1771

Garcia A. M., 1993, A&AS, 100, 47

Gerhard O. E., 1993, MNRAS, 265, 213

Gerssen J., Kuijken K., Merrifield M. R., 1997, MNRAS, 288, 618

Gerssen J., Kuijken K., Merrifield M. R., 1999, MNRAS, 306, 926

Hart L., Davies R. D., Johnson S. C., 1980, MNRAS, 191, 261

Hernquist L., Weinberg M. D., 1992, ApJ, 400, 80

Hunter J. H., Ball R., Huntley J. M., England M. N., Gottesman S. T., 1989, ApJ, 324, 721

Kent S. M., 1987, AJ, 93, 1062

King D. L., 1985, La Palma Technical Note, N 31

Kormendy J., 1985, ApJ, 292, L9

Knapen J. H., 1999, in Beckman J. E., Mahoney T. J., eds, ASP Conf. Ser. Vol. 187, The Evolution of Galaxies on Cosmological Timescales. Astron. Soc. Pac., San Francisco, p. 72

Knapen J. H., Shlosman I., Peletier R. F., 2000, ApJ, 529, 93

Laine S., 1996, PhD thesis, Florida University

Lauer T. R. et al., 1995, AJ, 110, 2622

Lindblad P. A. B., Kristen H., 1996, A&A, 313, 733

Lindblad P. A. B., Lindblad P. O., Athanassoula E., 1996, A&A, 313, 65

Little B., Carlberg R. G., 1991, MNRAS, 250, 161

Mayall N. U., de Vaucouleurs A., 1962, AJ, 67, 363

Merrifield M. R., Kuijken K., 1995, MNRAS, 274, 933

Miwa T., Noguchi M., 1998, ApJ, 499, 149

Möllenhoff C., Heidt J., 2001, A&A, 368, 16

Navarro J. F., Frenk C. S., White S. D. M., 1997, ApJ, 490, 493

Neistein E., Maoz D., Rix H.-W., Tonry J. L., 1999, AJ, 117, 2666

Nilson P., 1973, Uppsala General Catalogue of Galaxies. Royal Society of Sciences of Uppsala, Uppsala

Noguchi M., 1987, MNRAS, 228, 635

Osterbrock D. E., Fulbright J. P., Martel A. R., Keane M. J., Trager S. C., Basri G., 1996, PASP, 108, 277

Ostriker J. P., Peebles P. J. E., 1973, ApJ, 186, 467

Ohta K., Masaru H., Wakamatsu K., 1990, ApJ, 357, 71

Pogge R. W., Eskridge P. B., 1993, AJ, 106, 1405

Salo H., 1991, A&A, 243, 118

Sánchez-Portal M., Díaz Ángeles I., Terlevich R., Terlevich E., Álvarez Álvarez M., Aretxaga I., 2000, MNRAS, 312, 2

Sancisi R., van Woerden H., Davies R. D., Hart L., 1984, MNRAS, 210, 497

Sandage A., Tammann G. A., 1981, A revised Shapley-Ames Catalog of Bright Galaxies. Carnegie Institution of Washington, Washington DC

Schechter P. L., 1983, ApJS, 52, 425

Schelgel D. J., Finkbeiner D. P., Davis M., 1998, ApJ, 500, 525

Sellwood J. A., 1980, A&A, 89, 296

Sellwood J. A., Wilkinson A., 1993, Rep. Prog. Phys., 56, 173

Sellwood J. A., Evans N. W., 2001, ApJ, 546, 176

Sil'chenko O. K., 1999, AJ, 117, 2725

Simien F., Prugniel P., 1997, A&AS, 126, 519

Sofue Y., Wakamatsu K., Taniguchi Y., Nakai N., 1993, PASJ, 45, 43

Taniguchi Y., Murayama T., Nakai N., Suzuki M., Kameya O., 1994, AJ, 108, 468

Tonry J. L., Davis M., 1981, ApJ, 246, 666

Toomre A., 1981, in Fall S. M., Lynden-Bell D., eds, The Structure and Evolution of Normal Galaxies. Cambridge University Press, Cambridge, p. 111

Tremaine S., Weinberg M. D., 1984, ApJ, 282, L5

Tremaine S., Ostriker J. P., 1999, MNRAS, 306, 662

van Albada T. S., Sanders R. H., 1982, MNRAS, 201, 303

van Albada T. S., Sancisi R., 1986, Phil. Trans. R. Soc. Lond. A, 320, 447

van der Marel R. P., Franx M., 1993, ApJ, 407, 525

Weinberg M. D., 1985, MNRAS, 213, 451

Weiner B. J., Sellwood J. A., Williams T. B., 2001, ApJ, 546, 931

This paper has been typeset from a TeX/LaTeX file prepared by the author.